Total magnetic force on a ferrofluid droplet in microgravity

Romero-Calvo, Álvaro; Cano-Gómez, Gabriel; Hermans, Tim H.J.; Parrilla Benítez, Lidia; Herrada Gutiérrez, Miguel Ángel; Castro-Hernández, Elena

DOI
10.1016/j.expthermflusci.2020.110124

Publication date
2020

Document Version
Accepted author manuscript

Published in
Experimental Thermal and Fluid Science

Citation (APA)
Romero-Calvo, Á., Cano-Gómez, G., Hermans, T. H. J., Parrilla Benítez, L., Herrada Gutiérrez, M. Á., & Castro-Hernández, E. (2020). Total magnetic force on a ferrofluid droplet in microgravity. *Experimental Thermal and Fluid Science*, *117*, Article 110124. https://doi.org/10.1016/j.expthermflusci.2020.110124

Total magnetic force on a ferrofluid droplet in microgravity

Álvaro Romero-Calvo[a,b,*], Gabriel Cano-Gómez[c], Tim H. J. Hermans[d], Lidia Parrilla Benítez[b], Miguel Ángel Herrada Gutiérrez[b], Elena Castro-Hernández[b]

[a] *Department of Aerospace Engineering Sciences, University of Colorado Boulder, 429 UCB, 80303, Boulder, CO, US*
[b] *Área de Mecánica de Fluidos, Departamento de Ingeniería Aeroespacial y Mecánica de Fluidos, Universidad de Sevilla, Avenida de los Descubrimientos s/n 41092, Sevilla, Spain*
[c] *Departamento de Física Aplicada III, Universidad de Sevilla, Avenida de los Descubrimientos s/n 41092, Sevilla, Spain*
[d] *Astrodynamics & Space Missions, Delft University of Technology, Delft, The Netherlands*

Abstract

The formulation of the total force exerted by magnetic fields on ferrofluids has historically been a subject of intense debate and controversy. Although the theoretical foundations of this problem can now be considered to be well established, significant confusion still remains regarding the implementation of the associated expressions. However, the development of future applications in low-gravity environments is highly dependent on the correct modeling of this force. This paper presents a contextualized analysis of different proposed calculation procedures and validation in a space-like environment. Kinematic measurements of the movement of a ferrofluid droplet subjected to an inhomogeneous magnetic field in microgravity are compared with numerical predictions from a simplified physical model. Theoretical results are consistent with the assumptions of the model and show an excellent agreement with the experiment. The Kelvin force predictions are included in the discussion to exemplify how an incomplete modeling of the magnetic force leads to significant errors in the absence of gravity.

Keywords: Total magnetic force, ferrofluids, microgravity, magnetic mass transfer, space engineering

1. Introduction

The calculation of the total force exerted by electromagnetic fields on electrically or magnetically polarizable continuous media is a relevant problem of electromagnetism. Different procedures can be used to face this problem and, although the validity and equivalence between them is generally accepted, their associated physical models have become a subject of debate in the past.

The discussion has been particularly intense in what refers to the distribution of forces within a magnetic fluid. While in [1] it is considered that the action of an external field produces forces throughout the medium, in [2] it is concluded that only the surface exhibits a force distribution with true physical meaning. Further considerations on how magnetic fields contribute to the energy variation result in different formulations of this interaction [2–7].

A larger consensus exists in the different formulations of the *total force*. The subject was revisited in 2001 when the validity of the Kelvin force expression in ferrofluids was contested [3] and a significant response was produced [2; 4; 6; 8; 9]. Although this debate can be regarded as outdated, a review of recent publications unveils that the total force is not always formulated in a fully rigorous manner. Common simplifying assumptions are (i) the identification of the applied $\boldsymbol{H}_0$ and internal $\boldsymbol{H}$ magnetic fields, (ii) the elimination of the surface force components related to the normal or tangential discontinuities of the magnetization field, or (iii) the removal of the demagnetization field. For instance, in [10] an approximate model that neglects the contribution of magnetized liquid oxygen to the magnetic field is employed, while surface forces arising from the discontinuity in the magnetization field are directly ignored. Those surface components are also neglected in [11; 12], where only the Kelvin volume force density is considered. In [13; 14] the

*alvaro.romerocalvo@colorado.edu

small size of the ferrofluid medium justifies the calculation of the volume force density by means of simplified expressions in terms of the $\boldsymbol{B}$ field, but without mentioning the corresponding surface components. These simplifications may be appropriate under normal-gravity conditions, but may result in significant errors in the presence of a strong magnetic force. Unfortunately, most contributions do not explicitly refer to the simplifying assumptions behind their formulations, hence becoming a source of confusion for non-experts.

The correct formulation and implementation of the total magnetic force becomes particularly relevant for space engineering applications dealing with ferrofluids. Ferrofluids are colloidal suspensions of magnetic nanoparticles in a carrier liquid. Their invention aimed to enable an artificially imposed gravity environment in microgravity, hence easing the management of liquid propellants in space [15]. The basic equations governing the dynamics of ferrofluids were first presented by Neuringer and Rosensweig in 1964 [16], giving rise to the field of Ferrohydrodynamics [17]. A non-exhaustive list of applications in space includes thermomagnetic convection [18; 19], mass transfer [20], micropropulsion [21; 22] and magnetic liquid positioning [11; 23; 24]. Due to their enhanced magnetic susceptibility and the absence of gravity, the magnetic force acquires a major role and the impact of the aforementioned simplifications is hence increased.

In this paper, kinematic measurements of the translation of a ferrofluid droplet subjected to an inhomogeneous magnetic field in microgravity are compared with numerical computations from different models. The total force formulations are depicted together with the incomplete result that the Kelvin force alone would produce. The droplet was generated during a series of microgravity experiments performed at ZARM's drop tower in Bremen as part of the *Drop Your Thesis!* 2017 programme run by ESA Academy.

This work aims to provide: (i) a comprehensive review of the existing formulations for the total magnetic force, (ii) further evidence on their reliability and proper implementation, and (iii) an experimental example of magnetic mass transfer in microgravity in the midterm between typical laboratory setups and practical applications. The theoretical problem is analyzed in Section 2, Section 3 presents the microgravity experiment, Section 4 shows and discusses the results and Section 5 summarizes the main conclusions of the work.

2. Theoretical Background

The total force exerted by an electric or magnetic field on a polarizable medium has been formulated and solved by analyzing the variation of energy of the microscopic dipoles composing the material [25–28]. This general approach can be developed by following different methods [2; 8]: (i) calculation of the total force in terms of the *electromagnetic traction* on a surrounding boundary surface; (ii) calculation of the resultant of the system of distributed forces, and (iii) evaluation of the energy balance of the system by means of the principle of virtual works. These procedures are equivalent and, if correctly applied, must lead to the same result. From the physical viewpoint, however, they rely on different models of the system of distributed forces acting on the medium.

2.1. Total magnetic force derived from the Maxwell stress tensor

The aforementioned procedures (i) and (ii) employ the *Maxwell stress tensor* $\mathcal{T}_M$, which can be regarded as a powerful tool for describing the electrodynamic and electromagnetic forces acting on a continuous medium. In the general framework of electromagnetism, the Maxwell stress tensor has been introduced in several ways with different interpretations of its physical or merely mathematical meaning [17; 25–27; 29; 30].

In the case of electrically and/or magnetically polarized fluid media, where dissipative and electro/magnetostriction processes are considered, Maxwell equations and dynamic balance relationships (including linear momentum, angular momentum, energy and entropy production rate) lead to a general *pressure-viscous-electromagnetic* stress tensor scheme for $\mathcal{T}_M$ [2; 31].

In the present study, the material medium under analysis is electrically neutral and remains in thermodynamic equilibrium with constant density, temperature and chemical potentials. The stress tensor can be then formulated as

$$\mathcal{T}_M = -p\mathcal{I} + \mathcal{T}_m, \tag{1}$$

where $\mathcal{T}_m$ is the *magnetic stress tensor*, and the unit dyadic $\mathcal{I} = (\delta_{ij})$ is multiplied by a *pressure-like* variable p. The *canonical form* of the magnetic work per unit volume done to magnetize the

medium, $\boldsymbol{H}\cdot\delta\boldsymbol{B}$, leads to the magnetic stress tensor

$$\mathcal{T}_m = \boldsymbol{B}\boldsymbol{H} - \frac{\mu_0}{2}\, H^2\, \mathcal{I}, \tag{2}$$

with the first term being the dyadic resulting from the tensor product of the induction $\boldsymbol{B}$ and magnetic $\boldsymbol{H}$ fields, related through $\boldsymbol{B} = \mu_0(\boldsymbol{H} + \boldsymbol{M})$, and where $\boldsymbol{M}$ is the magnetization field. The magnetic stress tensor expressed in Eq. (2) has been widely used in classical and recent bibliography on electromagnetism to obtain the magnetic force on a magnetizable body [1; 8; 25; 29; 31]. Here it has been defined by grouping in Eq. (1) those terms of the magnetic work that exclusively contribute to the variation of the magnetic energy density. The corresponding *pressure-like* variable p is

$$p(\upsilon, T, H) = p_0(\upsilon, T) + \pi_m(H), \tag{3}$$

where $p_0(\upsilon, T)$ is the thermodynamic pressure in the absence of magnetic fields and $\upsilon = \rho^{-1}$ is the specific volume of the ferrofluid. The term

$$\pi_m(H) = \mu_0 \int_0^H \frac{\partial[\upsilon M]}{\partial \upsilon}\, \mathrm{d}H', \tag{4}$$

reflects the pressure change due to the interaction between magnetic dipoles.

An identical formulation of the Maxwell stress tensor for a magnetized medium in equilibrium is obtained in [2; 17] by applying a balance of magnetic work and free energy. However, it is arranged so that the above *magnetic pressure* term $\pi_m(H)$ is considered to be part of the magnetic stress tensor $\mathcal{T}_m$ from which the magnetic force distributions are later derived. Therefore, only the zero–field pressure $p_0(\upsilon, T)$ constitutes the pressure–like variable. These two definitions of $\mathcal{T}_m$ lead to different magnetic force distributions but, as shown in Subsection 2.1.3 and Appendix A, result in identical expression for the total force. In Ref. 17, Rosensweig emphasizes that the grouping of terms is arbitrary and may lead to confusion. Since in magnetically diluted ferrofluids it is commonly assumed that $M \sim \rho$, the contribution of $\pi_m(H)$ to the magnetic stress tensor is in any case negligible.

2.1.1. Resultant of the magnetic traction on the boundary

In this study, a volume V of a magnetizable and electrically neutral medium, immersed in a non-magnetic environment ($\boldsymbol{M} = \boldsymbol{0}$), is subjected to the action of an applied magnetostatic field $\boldsymbol{H}_0$ in microgravity. The resulting translation movement is due to the force distributions derived from the magnetic stress tensor $\mathcal{T}_m$. Assuming that the magnetized medium is in thermodynamic equilibrium, the total magnetic force can be computed by applying

$$\boldsymbol{F}_m^T = \oint_{\partial V} \mathrm{d}S\, (\boldsymbol{n}\cdot\mathcal{T}_m^+) \tag{5}$$

in the external surface ∂V^+ of the body, with $\boldsymbol{n}$ being the external normal vector [1; 2; 8; 25]. If the polarized body is surrounded by a non-magnetic and non-electric material, $\partial V'$ can be taken as any closed surface around it [2; 8]. In this framework, the term of magnetic pressure π_m^+ is strictly null in the surrounding medium. Therefore, Eq. (5) is not affected by its inclusion in the magnetic stress tensor.

Although the practical utility of Eq. (5) is recognized for the calculation of the total magnetic force, different interpretations of its physical meaning have been suggested. In [2] it is proposed that the actual forces acting on the polarized medium are located at the body surface. In contrast, the general validity of this procedure is discussed in [1], where no physical meaning is attributed to the Maxwell stress tensor. That is, it is not considered to be a true Cauchy stress tensor, then leading to a system of fictitious tensions. Finally, in [31] the *total pressure-viscous-electromagnetic stress tensor* is used to predict the existence of volume forces due to coupled polarization, and its experimental verification is proposed.

2.1.2. Resultant of the magnetic force distributions

The local effect of electromagnetic fields on continuous media can be formulated in terms of a body force determined by the divergence of the Maxwell stress tensor [17; 29; 30]. In the case of a magnetizable medium subjected to a magnetic field, the magnetic body force density is

$$\boldsymbol{f}_{m,V} = \nabla\cdot\mathcal{T}_m \quad \forall\, P \in V, \tag{6}$$

where P is a spatial position. This force density would then depend on the local magnetic field.

Since the tensor is discontinuous between the internal (∂V^-) and external (∂V^+) faces, a surface force density $f_{m,S}$ arises at ∂V [1; 2; 8; 17]

$$\boldsymbol{f}_{m,S} = \boldsymbol{n}\cdot\mathcal{T}_m^+ - \boldsymbol{n}\cdot\mathcal{T}_m^- \quad \forall\, P \in \partial V. \tag{7}$$

Therefore, the general expression of the total magnetic force calculated from this physical model is [1; 2; 5; 7–9].

$$\boldsymbol{F}_m = \int_V \mathrm{d}V\, \boldsymbol{f}_{m,V} + \oint_{\partial V} \mathrm{d}S\, \boldsymbol{f}_{m,S}, \qquad (8)$$

where $\boldsymbol{f}_{m,V}$ and $\boldsymbol{f}_{m,S}$ are given by Eqs. (6) and (7), respectively.

The mathematical equivalence between Eqs. (8) and (5) is immediate: the magnetic field and $\mathcal{T}_m$ are continuous in V, so the divergence theorem leads to

$$\int_V \mathrm{d}V\, (\nabla \cdot \mathcal{T}_m) = \oint_{\partial V} \mathrm{d}S\, (\boldsymbol{n} \cdot \mathcal{T}_m^-), \qquad (9)$$

where the second term is evaluated in the internal face of ∂V. If this identity is applied to Eq. (8) considering Eqs. (6) and (7), Eq. (5) is obtained.

Only the magnetic contribution of the Maxwell stress tensor formulated in Eq. (1) is employed for the calculation of the magnetic force densities given by Eqs. (6) and (7), or the corresponding surface density in Eq. (5). However, the pressure term must be considered in the determination of the equilibrium surface ∂V, and hence in the resultant forces shown in Eqs. (5) or (8).

2.1.3. Expressions for the resultant of the distributions of forces

The magnetic fluid in equilibrium exhibits the behavior of a soft magnetic material, so that local magnetic fields are collinear. The *natural* constitutive relation that macroscopically characterizes the magnetized fluid would then be $\boldsymbol{M} = \chi(H)\, \boldsymbol{H}$, where χ is the magnetic susceptibility.

The application of Eq. (6) to the canonical form in Eq. (1), together with some elementary vector-dyadic identities, results in the corresponding magnetic body-force density

$$\boldsymbol{f}^H_{m,V} = \mu_0 (\boldsymbol{M} \cdot \nabla)\boldsymbol{H} = \mu_0\, M \boldsymbol{\nabla} H, \qquad (10)$$

where, due to the absence of electric currents in the volume of the magnetized medium, $\nabla \times \boldsymbol{H} = \boldsymbol{0}$ in V. The above expression is usually known as *Kelvin force*.

The corresponding surface-force density $\boldsymbol{f}^H_{m,S}$ in ∂V is obtained by applying Eq. (7). It should be noted that, according to Gauss's law, the normal component of the induction field is continuous through the interface ($B_n^+ = B_n^- = B_n$). In addition, the absence of electrical surface currents in ∂V results in the continuity of the tangential magnetic field component ($H_t^+ = H_t^- = H_t$). The result is

$$\boldsymbol{f}^H_{m,S} = \frac{\mu_0}{2}\, M_n^2\, \boldsymbol{n}, \qquad (11)$$

being M_n the normal magnetization component at ∂V^-. By making use of Eq. (8), the total magnetic force becomes

$$\boldsymbol{F}^H_m = \mu_0 \int_V \mathrm{d}V M \nabla H \; + \frac{\mu_0}{2} \oint_{\partial V} \mathrm{d}S\, M_n^2\, \boldsymbol{n}, \qquad (12)$$

This expression has been applied in [7; 9], showing that the volume term corresponding to the Kelvin force must be completed by the surface term. It has also been proposed in [2] as one of the equivalent forms of the total magnetic force acting on a magnetized fluid in vacuum, but considering that the volume term belongs to a force distribution physically located at the surface.

The magnetic and pressure stress tensors given by Eqs. (2) and (3) can be defined with the *Cowley-Rosensweig* formulation, that includes the integral term $\pi_m(H)$ in the magnetic tensor [17]. The Appendix A shows how this leads to different volume and surface force distributions and the same total force expression.

Eqs. (2) and (3) are not, however, the only proposed form of the total stress tensor presented in Eq. (1). In [3; 32] the magnetic body-force density given by Eq. (15) is derived assuming a constitutive relation in terms of the induction field $\boldsymbol{M} = \tilde{\chi}(B)\, \boldsymbol{B}/\mu_0$, where $\tilde{\chi}$ is an alternative definition of the magnetic susceptibility. The total stress tensor corresponding to this volume distribution is obtained in Ref. 2 assuming that the differential contribution of the magnetic work to the local energy distribution in the polarizable medium is $-\boldsymbol{B} \cdot \delta \boldsymbol{H}$. Dual expressions are then obtained for the magnetic and pressure stress tensors [2; 5]

$$\mathcal{T}_m = \boldsymbol{B}\boldsymbol{H} - \frac{\mu_0}{2}\, [H^2 - M^2]\, \mathcal{I}, \qquad (13)$$

$$p(\upsilon, T, B) = p_0(\upsilon, T) + \int_0^B \frac{\partial [\upsilon M]}{\partial \upsilon}\, \mathrm{d}B', \qquad (14)$$

where, as in Eq. (2), the magnetic tensor is built only from terms which are directly related to the variation of the magnetic energy density in the medium. The divergence of Eq. (13) in V and its discontinuity in ∂V produce the volume and surface densities associated with this dual form. Applying Eq. (6) and Eq. (7) and considering again

the absence of electric currents in V and ∂V, the magnetic body force $\boldsymbol{f}^B_{m,V}$ and surface force $\boldsymbol{f}^B_{m,S}$ densities are

$$\boldsymbol{f}^B_{m,V} = (\boldsymbol{M}\cdot\nabla)\boldsymbol{B} + \mu_0 \boldsymbol{M}\times(\nabla\times\boldsymbol{M}) = M\nabla B, \tag{15}$$

$$\boldsymbol{f}^B_{m,S} = -\frac{\mu_0}{2}\, M_t^2\, \boldsymbol{n}. \tag{16}$$

with M_t being the tangential magnetization component at ∂V^-. The expression for the resulting magnetic force derived from the dual form of the magnetic stress tensor is then

$$\boldsymbol{F}^B_m = \int_V \mathrm{d}V\, M\nabla B \; - \frac{\mu_0}{2}\oint_{\partial V} \mathrm{d}S\, M_t^2\, \boldsymbol{n}. \tag{17}$$

This dual formulation gives rise to different distributions of forces with respect to the canonical form. However, in Appendix B it is shown that both approaches are equivalent in terms of the total magnetic force acting on a volume V of magnetized fluid, and then also to the resultant of the magnetic traction in the boundary given by Eq. (5). To the best knowledge of the authors, this demonstration has not been presented in previous works.

The magnetic term in Eq. (14), $\tilde{\pi}_m(B) = \int_0^B \partial[\nu M]/\partial\nu d B'$, may be included in the magnetic tensor to obtain the corresponding force distributions. Following the procedure developed in the Appendix A, it is found that although the resulting magnetic force densities differ from Eqs. (15) and (16), they lead to the same total magnetic force expressed in Eq. (17).

2.2. Energy balance and virtual works scheme

The free energy variation δF of a magnetizable medium due to changes in the applied magnetic field $\boldsymbol{H}_0$ is given by [25]

$$\delta F = -\mu_0 \int_V \mathrm{d}V\, \boldsymbol{M}\cdot\delta\boldsymbol{H}_0. \tag{18}$$

If this variation is due to the displacement of the body in a non-magnetic environment with respect to the applied magnetic field $\boldsymbol{H}_0$, then $\delta\boldsymbol{H}_0 = (\delta\boldsymbol{r}\cdot\nabla)\boldsymbol{H}_0$. Assuming that the displacement is not caused by other interactions, the application of the principle of virtual works results in the total magnetic force [4; 8; 25]

$$\boldsymbol{F}^0_m = \mu_0 \int_V \mathrm{d}V\, (\boldsymbol{M}\cdot\nabla)\boldsymbol{H}_0. \tag{19}$$

It should be noted that this formulation does not add information about the stresses in the body.

If the thermodynamic equilibrium condition is verified for a system involving magnetized fluids in a non-magnetizable environment and subjected to an external magnetic field, the energy-balance-based total force expression given by Eq. (19) must give the same result as Eq. (5) and, therefore, as Eq. (12) or Eq. (17) [2; 4; 8]. The demonstration of this equivalence is given in Section 3.3 of Ref. 2.

The procedure formulated in Eq. (19) can be considered as the most straightforward method to compute the total force on a magnetically polarized body. Its application to magnetized fluids is restricted to the condition of thermodynamic equilibrium, discarding any process characterized by significant magnetostrictive or magnetodisipative effects. For non-equilibrium processes, procedures involving the Maxwell stress tensor are recommended instead [8].

In order to set a correct validity range, it is convenient to develop a criteria to verify the magnetostatic condition, and hence the equivalence between the proposed procedures.

2.3. Magnetostatic Conditions

When the applied magnetic field varies, the microscopic dipoles inside the ferrofluid shift to a new equilibrium position. This process occurs by means of two mechanisms: the Brownian relaxation involving a physical rotation of the dipoles, and the Néel relaxation associated with a rotation of the magnetic dipoles within the particles. Each process is respectively characterized by a relaxation time τ_B and τ_N with an effective relaxation time τ given by [33]

$$\frac{1}{\tau} = \frac{1}{\tau_B} + \frac{1}{\tau_N}. \tag{20}$$

Any process satisfying the magnetostatic hypothesis must have a characteristic time significantly larger than τ to allow an instantaneous reorientation of the dipoles. If the ferrofluid is moving in an inhomogeneous and static magnetic field, the characteristic time of change of the field may be computed as

$$\tau_f = \frac{H_{ref}}{v_f \nabla H}, \tag{21}$$

where H_{ref} is a reference value of the magnetic field intensity and v_f is the velocity of the ferrofluid volume. If the ratio τ_f/τ is greater than 1, the magnetostatic hypothesis can be assumed as valid.

2.4. Summary of total force formulations

For the sake of clarity, the equivalent formulations of the total magnetic force on ferrofluids derived in this section are summarized in Table 1. The volume term of $\boldsymbol{F}_m^H$, named Kelvin force and identified by $\boldsymbol{F}_{m,V}^H$, is computed separately in Section 4 to exemplify how incomplete formulations lead to wrong predictions even for low-susceptibility ferrofluids.

3. Microgravity experiment

Once the equivalence between Eq. (5), Eq. (12), Eq. (17) and Eq. (19) has been verified, it is convenient to address their applicability and numerical implementation. A comparison with experimental results offers an insight into the validity and robustness of those procedures under reasonable simplifications.

Measurements of the total force on ferrofluids have been traditionally obtained by means of long pendulum setups where the magnetic force was compensated with the action of gravity [3; 9]. In the case under analysis, however, the generation of a floating ferrofluid droplet in microgravity is used for that purpose. This has the potential advantage of enabling a high-quality three-dimensional observation of the kinematics of the ferrofluid volume while subjected to an arbitrary magnetic field.

3.1. Experiment Setup

The experiment here presented is framed in the *ESA Drop Your Thesis!* 2017 campaign, that studied the free axisymmetric oscillations of a ferrofluid solution in a cylindrical vessel in microgravity [34]. The drop tower setup, represented in Figure 1, was designed to impose a vertical percussion to the ferrofluid container and measure the deformation of the free surface. 9.3 seconds of microgravity conditions were achieved by making use of ZARM's drop tower catapult mode.

Table 1: Equivalent total magnetic force expressions

Symbol	Volume term	Surface term
$\boldsymbol{F}_m^T$	-	$\boldsymbol{n}\cdot\mathcal{T}_m^+$
$\boldsymbol{F}_m^H$	$\mu_0 M\nabla H$	$\mu_0 M_n^2\boldsymbol{n}/2$
$\boldsymbol{F}_m^B$	$M\nabla B$	$-\mu_0 M_t^2\boldsymbol{n}/2$
$\boldsymbol{F}_m^0$	$\mu_0(\boldsymbol{M}\cdot\nabla)\boldsymbol{H}_0$	-

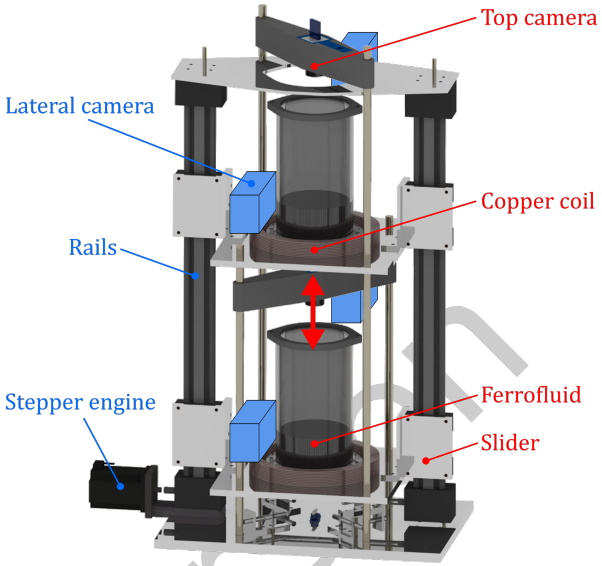

Figure 1: Experiment setup. The fixed and sliding assemblies are labeled in blue and red, respectively. The red arrow shows the movement induced by the percussion mechanism on the sliding assembly.

The experiment setup is composed of a Plexiglas vessel that contains a ferrofluid, a circular copper coil located at its base and a pair of cameras. This assembly is duplicated 368 mm below. The Plexiglas vessels have an inner diameter of 110 m, a height of 200 mm and are filled up to 50 mm by 475 ml of the EMG-700 ferofluid solution described in Section 3.3. The coils are connected in series and have 200 windings of a 1.8 mm diameter wire, an inner diameter of 160 mm and a width of 31 mm. A constant intensity power source working at 16.1 A feeds the coils during the experiment. Two GoPro Hero 5 Session cameras are located at approximately opposite sides of the vessel and work at 60 fps, 1920×1080 px^2 resolution and wide FOV. In order to start a free surface oscillation, a stepper engine imposes a vertical percussion to the setup 4.5 s after launch, as sketched in Figure 1. Further details on the experimental setup can be found in Refs. 34 and 35.

During the fourth drop of the ESA *Drop Your Thesis!* 2017 campaign, the vertical percussion produced by the stepper engine generated a ferrofluid jet and a floating droplet of 11 mm diameter in the upper assembly. This effect was not observed in the other four drops and is a consequence of the destabilization of the free surface. From the classical low-gravity sloshing theory perspective, the desta-

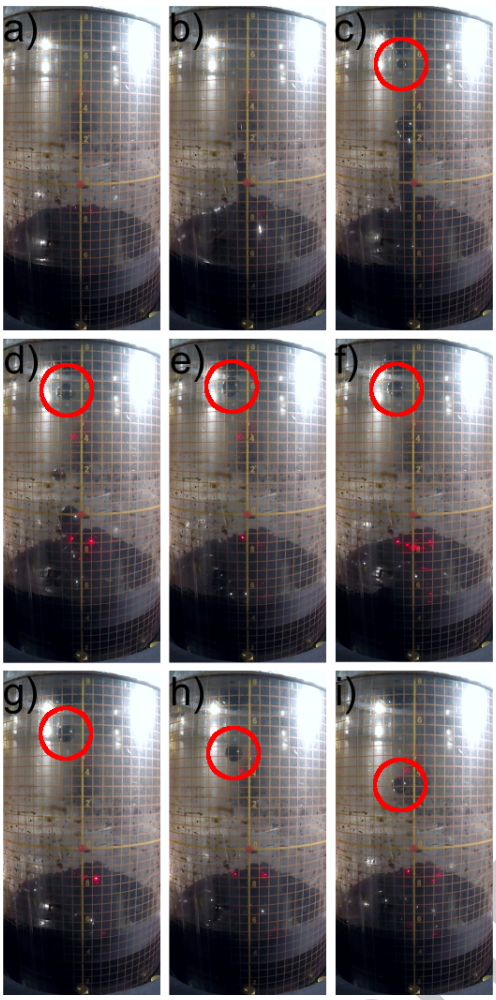

Figure 2: Sequence captured by Camera 1 showing the ferrofluid droplet formation and evolution after the application of the vertical percussion. a) t=-2.5 s; b) t=-1 s; c) t=-0.5 s; d) t=0 s; e) t=0.5 s; f) t=1 s; g) t=1.5 s; h) t=2 s; i) t=2.5 s.

bilization is produced when the critical acceleration (or critical Bond number) is reached [36]. Figure 2 represents the formation and breakup of the ferrofluid jet, that generated several droplets of different sizes. Only one of them, surrounded by a red circle, could be tracked with reasonable accuracy. Surface oscillations were induced by the percussion, but, as shown in Appendix C, their impact on the magnetic field can be considered negligible.

3.2. Droplet tracking system

The position of the droplet is triangulated by making use of the two lateral cameras of the upper assembly (see Figure 1). After correcting the intrinsic image deformation by means of Scaramuzza's camera model [37] and synchronizing both video signals, a circle is manually fitted to the contour of the droplet to obtain the approximate position $\{x_i', z_i'\}$ of the center of mass in the image axes. The process is repeated for each video frame. These measurements are then converted to their corresponding spherical angles, which are referred to the optical axis. Employing a pinhole camera model, the spherical angles are

$$\beta_i^x = \frac{x_i'}{R_x} \cdot FOV_x, \quad \beta_i^z = \frac{z_i'}{R_z} \cdot FOV_z, \tag{22}$$

where $i = 1, 2$ identifies the camera, R_j is the image resolution, and FOV_j is the field of view. Finally, a 5 (z) and 4 (x) degree polynomial interpolation is employed to filter the manual measurements.

A right Cartesian reference system $\{\hat{\boldsymbol{x}}, \hat{\boldsymbol{y}}, \hat{\boldsymbol{z}}\}$ located at the base of the container and represented in Figure 3 defines the world coordinates of the droplet. The $\hat{\boldsymbol{z}}$ axis is coincident with the axis of symmetry, while the $\hat{\boldsymbol{x}}$ and $\hat{\boldsymbol{y}}$ axes are aligned with the square platform shown in Figure 1. It is convenient to first determine the coordinate y, which based on Figure 3 is given by

$$tan(\beta_1^z - \alpha_1^z)(d_1 + y) - tan(\beta_2^z - \alpha_2^z)(d_2 - y) + \Delta h = 0, \tag{23}$$

where α_i^z is the vertical inclination error, d_i is the distance between the optical center and the mean plane, $\Delta h = h_1^z - h_2^z$, and h_i^z is the height with respect to the base of the container. Due to the uncertainty in the geometric parameters, the error in the determination of y increases when the droplet gets closer to the line of sight that connects both cameras. However, artifacts are minimized if both videos are correctly synchronized.

Once the depth is known, the z coordinate is given by

$$z = tan(\beta_1^z - \alpha_1^z) \cdot (d_1 + y) + h_1^z. \tag{24}$$

The process is analogous for the x coordinate, where

$$x = tan(\beta_1^x - \alpha_1^x) \cdot (d_1 + y) + h_1^x, \tag{25}$$

and h_1^x is the lateral displacement of the camera in the x axis. The droplet acceleration values are obtained by applying a central finite difference scheme to the filtered position values.

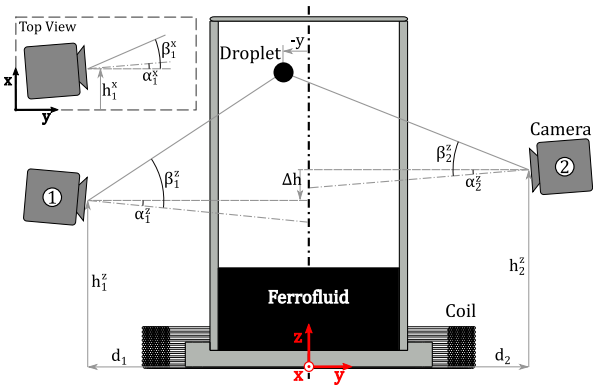

Figure 3: Upper vessel and sketch of the visualization system

The parameters of the droplet tracking system and their tolerances are given in Table 2. The lasts are a conservative estimation based on the measurement instruments and, in the case of the tilting angles, on indirect image analysis procedures. The tolerance in sensible parameters is increased to account for the relaxation of the experiment setup in the absence of gravity.

A Monte Carlo simulation is carried out to estimate the error of the visualization system. Each geometric parameter listed in Table 2 is perturbed with an additive white Gaussian noise by identifying the measurement tolerance with the 3σ interval. The fitting error in β_i^x and β_i^z, whose standard deviation ranges from 0.04° to 0.06°, is also considered. This set of perturbed parameters and variables is fed into Eqs. (22) to (24) to obtain the droplet position and acceleration. The droplet tracking system error is finally determined by computing the standard deviation of the full Monte Carlo dataset for the desired variables. 2500 simulations are performed, that converge to the standard deviation of the position with a rate of less than a 0.05%.

The uncertainties in the experimental droplet position also define the standard deviation of the total force expressions listed in Table 1. The magnetic field is determined with a standard deviation error of ±3% and contributes to this effect.

3.3. Ferrofluid properties

The commercial Ferrotec EMG-700 water-based ferrofluid is diluted in a 1:10 volume solution of demineralized water (0.58% volume concentration). Density $\rho = 1.020 \pm 0.003$ g/ml, viscosity $\mu = 1.448 \pm 0.007$ cP and surface tension $\sigma = 61.70 \pm 0.95$ mN/m are measured. The magnetization curve, measured with MicroSense EZ-9 Vibrating Sample Magnetometer, is represented in Figure 4 and shows an initial susceptibility $\chi = 0.181$ and saturation magnetization $M_s = 3160$ A/m.

Table 2: Droplet tracking system parameters

Symbol	Value	Tolerance	Units
R_x	1080	-	px
R_z	1920	-	px
FOV_x	58.7	±0.5	deg
FOV_z	96.2	±0.5	deg
α_1^x	-1.7	± 2.2*	deg
α_1^z	-1.3	± 1.3*	deg
α_2^z	-1.3	± 1.3*	deg
d_1	199	±2	mm
d_2	201	±2	mm
h_1^z	143	±3*	mm
h_2^z	146	±3*	mm
h_1^x	0	±2	mm

* Increased to account for structure relaxation.

The 10 nm nanoparticles of the ferrofluid solution are made of magnetite (Fe_3O_4) and are coated with an anionic surfactant. Their relaxation time is estimated to be $\tau \approx 5 \cdot 10^{-9}$ s [33].

4. Results & Discussion

The magnetic field $\boldsymbol{H}_0$ applied to the ferrofluid droplet is produced by the coils and the magnetized ferrofluid volume that remains at the base of the vessel. This system is approximated by means of a 2D axisymmetric Comsol Multiphysics finite

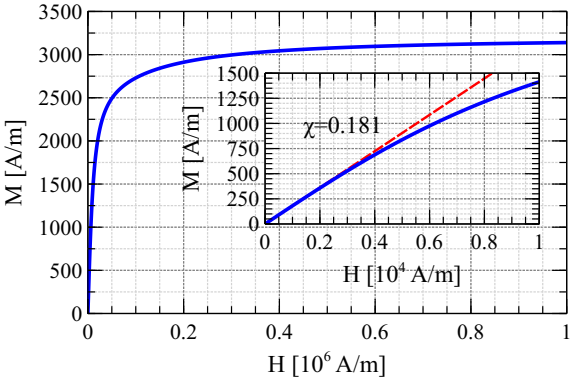

Figure 4: Measured magnetization curve of the 1:10 EMG-700 ferrofluid solution.

elements model. The internal fields $\boldsymbol{H}$ and $\boldsymbol{M}$ are computed from $\boldsymbol{H}_0$ by assuming that (i) the droplet is spherical with a demagnetization factor $D = 1/3$, (ii) the fields $\boldsymbol{H}$, $\boldsymbol{M}$ and $\boldsymbol{H}_0$ are collinear, and (iii) the internal dipoles are reoriented in a thermodynamic quasi-equilibrium process. The different total force formulations can be easily integrated in the droplet volume from these results. A detailed explanation of the numerical model can be found in the Appendix C.

The droplet projections in the cameras axes and their corresponding interpolations are first presented in Figure 5. The measurement error is more relevant in the x_i component, as the movement of the droplet is mainly produced in the $\hat{z}$ axis.

Figure 6 represents the position of the droplet as a function of time in the Cartesian reference system. The proximity to the vertical mid plane of the image and the lower accuracy associated to the lateral geometric parameters result in an uncertain measurement of x in Figure 6(a). The depth y is not affected by those factors, since it is estimated from β_i in Eq. (23). However, the errors in β_i have a significant impact on y, as shown in Figure 6(b).

Three axis acceleration values are derived from the position of the droplet with the aforementioned central finite differences scheme. The result is depicted in Figure 7 and detailed in Table 3 with predictions of the total magnetic force per unit mass given by the different formulations: $\boldsymbol{F}_m^T$ and $\boldsymbol{F}_m^0$ denote the values given by Eq. (5) and Eq. (19), respectively; Eq. (12) and Eq. (17) produce the same output, which is marked with the label "$\boldsymbol{F}_m^H$ *or* $\boldsymbol{F}_m^B$". Theoretical predictions are presented with an error band determined by the uncertainty in the droplet position and magnetic field model, which shows standard deviations of a 3% of the $\boldsymbol{H}_0$ module when compared with actual measurements. The high relative error in the lateral measurements results in an unreliable estimation of the lateral components. Higher errors are clearly observed around $t = 2.4$ s corresponding to the singularity in the line of sight between the cameras. Large uncertainties are also depicted at the beginning of the flight due to the mathematical derivation of the polynomials in the Monte Carlo analysis. Vertical accelerations, however, agree well with the theory. This is consistent with the relative uniformity of the vertical magnetic field component near the axis of symmetry, being less affected by radial uncertainties.

Since Eq. (5), Eq. (12), Eq. (17) and Eq. (19) are equivalent, the numerical discrepancies between them should be attributed to the simplifications in-

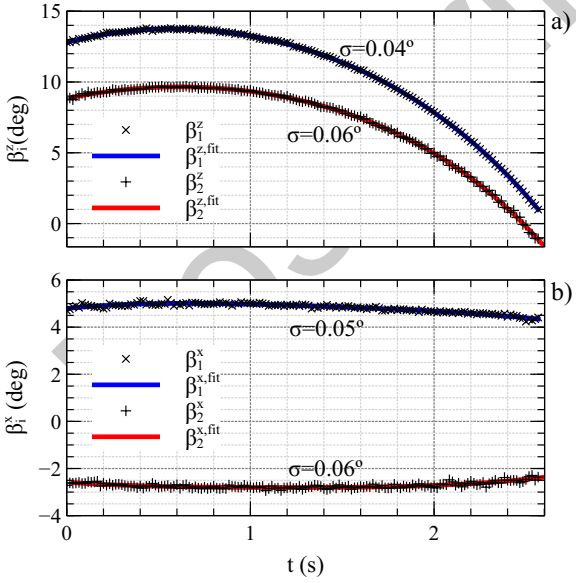

Figure 5: Droplet angles in cameras 1 and 2. Polynomials with degree 5 and 4 are employed to filter the (a) β_i^z and (b) β_i^x angles, respectively. The measurement error is quantified with the standard deviation σ.

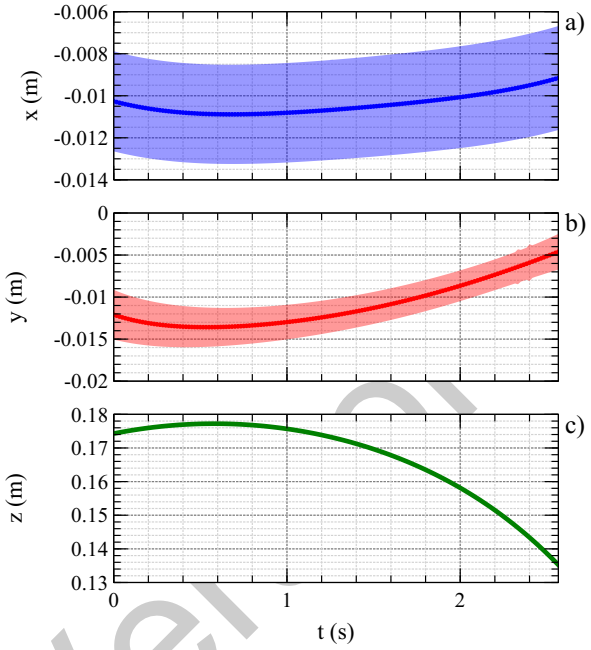

Figure 6: Position of the ferrofluid droplet as a function of time. The error bands represent the standard deviation. (a) x component, (b) y component, (c) z component

Table 3: Theoretical and experimental vertical acceleration values (in mm/s^2) according to the formulations given by Eq. (5), Eq. (10), Eq. (12), Eq. (17) and Eq. (19) as a function of time and the applied magnetic field in the center of the droplet. The error bands are represented by the standard deviation.

t (s)	0	0.5	1	1.5	2	2.5
H_0 (A/m)	2445 ± 73	2345 ± 70	2395 ± 72	2607 ± 78	3078 ± 92	4114 ± 123
F_m^T/m_d	-17.5 ± 1.4	-16.1 ± 1.3	-16.8 ± 1.3	-20.1 ± 1.6	-28.3 ± 2.2	-50.2 ± 3.6
$F_{m,V}^H/m_d$	-16.8 ± 1.4	-15.4 ± 1.2	-16.1 ± 1.3	-19.3 ± 1.6	-27.5 ± 2.2	-50.4 ± 3.9
F_m^H/m_d	-17.9 ± 1.4	-16.4 ± 1.3	-17.2 ± 1.4	-20.6 ± 1.6	-29.3 ± 2.3	-53.3 ± 4.1
F_m^B/m_d	-17.9 ± 1.4	-16.4 ± 1.3	-17.2 ± 1.4	-20.6 ± 1.6	-29.3 ± 2.3	-53.3 ± 4.1
F_m^0/m_d	-17.8 ± 1.4	-16.3 ± 1.3	-17.0 ± 1.4	-20.4 ± 1.6	-29.0 ± 2.3	-53.0 ± 4.0
Exp.	-17.5 ± 2.4	-17.4 ± 0.3	-17.9 ± 0.3	-21.5 ± 0.3	-31.0 ± 0.3	-50.4 ± 2.0

troduced in the physical model: (i) the assimilation of the droplet geometry to a sphere, and (ii) the approximation of $\boldsymbol{H}$ given by Eq. (C.8), where a constant demagnetization factor D is assumed. As indicated in the Appendix C and illustrated by Figure C.10, the size of the droplet and the smoothness of the magnetic field in the region under analysis justify those assumptions. The first has a similar impact on every calculation procedure, but the effects of the second depend on the formulation. While Eq. (12), Eq. (17) and Eq. (19) compute the fields in the magnetized volume, Eq. (5) only employs the value of $\boldsymbol{M}$ at the surface. Similarly, Eq. (5), Eq. (12) and Eq. (17) make use of the fields $\boldsymbol{M}$, $\boldsymbol{H}$ and $\boldsymbol{B}$, but Eq. (19) only requires $\boldsymbol{M}$. A different effect of approximation (ii) on the total force values from each formulation should then be expected for different sets of parameters, like initial susceptibility or droplet size. As observed in Figure 7, however, the discrepancies are not significant due to the reduced size of the droplet. It should be noted that the expression for $p = p(\upsilon, T, H)$ in Eq. (3) or $p = p(\upsilon, T, B)$ in Eq. (14), reflects the contribution of the magnetic field to the shape of the magnetic fluid volume, which will have an influence on the total force acting on the medium.

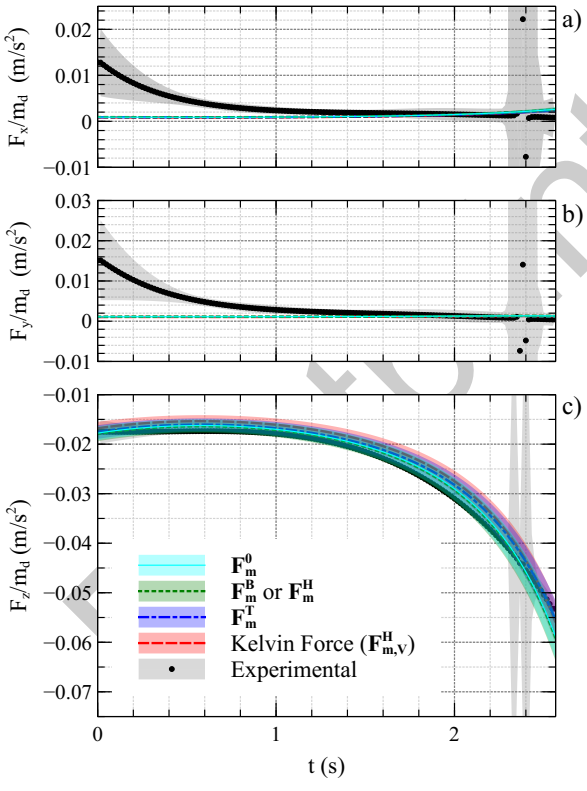

Figure 7: Experimental acceleration and theoretical forces per unit mass as a function of time. Theoretical values were computed based on Eq. (5), Eq. (12), Eq. (17) and Eq. (19) for a spherical droplet geometry. The error bands represent the standard deviation. (a) x component, (b) y component, (c) z component

Although the aforementioned simplifications may contribute to the discrepancy between theoretical and experimental values, the uncertainties associated to the droplet tracking system or the electromagnetic parameters play a more significant role, as shown by the error bands. In terms of the slope, however, it can be observed how experimental and theoretical values have a similar behavior in the first 1.4 seconds of flight. When the droplet is subjected to a stronger magnetic field ($t > 1.4$ s), the slopes predicted by Eq. (12), Eq. (17) and Eq. (19) diverge from the experimental ones. The results given by Eq. (5), on the contrary, show a better agreement. Again, this may be related with the impact of the approximation (ii) on each expression.

The integration of the Kelvin force density given by Eq. (10) in V, denoted by $\boldsymbol{F}_{m,V}^H$ and corresponding to the volume part of Eq. (12), is also repre-

sented for comparison. Although the differences between the predictions from that term and the total force in Eq. (12) may seem insignificant in Figure 7 or Table 3, their long-term effect is not. The theoretical acceleration profiles are integrated starting from the initial position and velocity of the droplet and compared with experimental measurements in Figure 8. The error band in the theoretical predictions is due to the uncertainty in the initial position and magnetic field model. The initial velocity is assumed to be known. The laws of motion $z(t)$ predicted by Eq. (5), Eq. (19), Eq. (12) or Eq. (17) show the best agreement with the experimental results and deviate from the prediction given by the Kelvin force $\boldsymbol{F}^{H}_{m,V}$, that falls outside the experimental error band.

5. Conclusions

This work presents the formulations of the total magnetic force on magnetic liquids and demonstrates their mathematical equivalence. Their implementation and performance are addressed by analyzing the movement of a ferrofluid droplet subjected to a static magnetic field in microgravity.

As expected, the formulations based on the Maxwell stress tensor in Eqs. (5), (12) and (17) or on the free energy balance given by Eq. (19) correctly approximate the kinematics of the ferrofluid droplet, while the Kelvin force density predictions deviate significantly. The similarity between these results is a consequence of the low susceptibility of the ferrofluid solution ($\chi = 0.181$), close to that of paramagnetic and diamagnetic liquids. Greater divergences may be observed with highly concentrated ferrofluids, where $\chi > 1$ [7; 9]. The indiscriminate use of Kelvin's force (or its dual expression) without the corresponding surface term may consequently lead to large errors when computing the total force. This assumption, common in normal-gravity research [12–14], has a critical impact in space applications, where the magnetic force acquires an overwhelming role due to the absence of gravity. Special care should then be taken when modeling, implementing and describing the magnetic interaction.

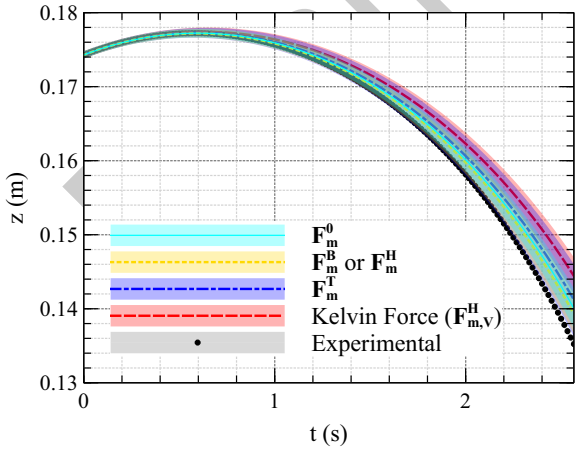

Figure 8: Measured and simulated height of the droplet as a function of time for the formulations given in 12, 17 and 19. The error bands represent the standard deviation.

The small differences between the numerical values given by Eq. (5), Eq. (12) or Eq. (17) and Eq. (19) are due to the assumptions in the calculation of $\boldsymbol{H}$. The results converge if the droplet size is small with respect to the characteristic length of variation of the magnetic field. Otherwise, the equilibrium shape of the droplet will play an important role in the calculation of the total magnetic force. Future work could investigate how those differences evolve for larger droplets if the previous assumptions are kept.

Besides the validation of the theoretical framework, this experiment presents an example of magnetic mass transport in space-like environments. The dynamics of the droplet are predicted with high accuracy despite the inherent complexity of the magnetic setup, conceptually close to real implementations. Therefore, applications dealing with the control of magnetic liquids in low-gravity environments may benefit from this contribution.

6. Competing Interests

The authors declare no competing interests.

7. Funding Sources

This work was supported by the European Space Agency Education Office and the Center of Applied Space Technology and Microgravity [ESA *Drop Your Thesis!* 2017 Programme]; the University of Seville [VI Plan Propio de Investigación y Transferencia]; and the research groups TEP-219 and TEP-956 of ETSI-Sevilla.

8. Acknowledgements

The authors thank the ESA Education Office for its financial, administrative, and academic support, ZARM for its technical assistance, the University of Seville for its academic supervision and financial contribution in the context of the VI Plan Propio de Investigación y Transferencia, the research groups TEP-219 and TEP-956 of ETSI-Sevilla for their financial support, the Aerospace Engineering Department and the Applied Physics III Department of ETSI-Seville for granting access to their facilities, TU Delft for its academic supervision, IGUS for its financial and technical support, and Álava Ingenieros for lending the visualization material. The authors would like to express their gratitude to the individuals of the aforementioned institutions who supported the ESA DYT 2017 *The Ferros* project.

Appendix A. Cowley-Rosensweig formulation

The magnetic stress tensor can be defined to include all the magnetic terms in Eq. (1), so that the pressure–like variable is identified with the zero–field pressure [17]. The expressions of Eqs. (2) and (3) are then reformulated as:

$$\mathcal{T}_m^{CR} = \boldsymbol{B}\boldsymbol{H} - \left[\pi_m(H) + \frac{\mu_0}{2}\, H^2\, \mathcal{I}\right], \tag{A.1}$$

$$p^{CR}(\upsilon, T) = p_0(\upsilon, T). \tag{A.2}$$

By applying Eqs. (6) and (7), the new volume and surface force densities are

$$f_{m,V}^{CR} = \mu_0 M \nabla H - \nabla \pi_m, \tag{A.3}$$

$$f_{m,S}^{CR} = \frac{\mu_0}{2} M_n^2 \boldsymbol{n} + \pi_m^- \boldsymbol{n} \tag{A.4}$$

These force densities are different from those expressed in Eqs. (10) and (11). If the resultant of these distributions is calculated according to the general expression Eq. (8) and the corollary of the divergence theorem for the gradient of a scalar field

$$\int_V \mathrm{d}V\, (\nabla \pi_m) = \oint_{\partial V} \mathrm{d}S\, (\pi_m^- \boldsymbol{n}) \tag{A.5}$$

is applied, the expression of the total force given by Eq. 12 is obtained. Ultimately, this demonstrates that the magnetic pressure term $\pi_m(H)$ is associated to the dipole interaction forces; that is, a distributed system of internal forces that alters the shape of the liquid interface, but does not produce a net force.

Appendix B. Equivalence of total magnetic forces

The dual expression in Eq. (15) for the magnetic body force and Kelvin force given by Eq. (10) differ in V by

$$\boldsymbol{f}_{m,V}^B - \boldsymbol{f}_{m,V}^H = M\nabla B - \mu_0 M \nabla H = \frac{\mu_0}{2}\, \nabla(M^2) \neq \boldsymbol{0}, \tag{B.1}$$

which is, in general, a non-zero term. The surface distributions are also locally different because

$$\boldsymbol{f}_{m,S}^B - \boldsymbol{f}_{m,S}^H = -\frac{\mu_0}{2}\, (M_t^2 + M_n^2)\boldsymbol{n} = -\frac{\mu_0}{2} M^2 \boldsymbol{n} \neq \boldsymbol{0}. \tag{B.2}$$

This result leads to a clear discrepancy in the local magnetic interaction. However, the symmetrical roles played by $\boldsymbol{H}$ and $\boldsymbol{B}$ in thermodynamics should be reflected in the magnetic force expression, so an *a priori* choice of one of the two forms would be unjustified [5].

If Eq.(B.1) and (B.2) are integrated respectively in the volume and the surface of the magnetized medium and then added, the equivalence of the total magnetic force derived from the canonical (12) and dual (17) formulations is obtained

$$\boldsymbol{F}_m^B - \boldsymbol{F}_m^H = \frac{\mu_0}{2} \left[\int_V \mathrm{d}V \nabla(M^2) - \oint_{\partial V} \mathrm{d}S M^2 \boldsymbol{n}\right] = \boldsymbol{0}. \tag{B.3}$$

Appendix C. Numerical Model

The applied magnetic field $\boldsymbol{H}_0$ to which the droplet is subjected is computed in Comsol Multiphysics by solving the stationary Maxwell equations

$$\nabla \times \boldsymbol{H}_0 = \boldsymbol{J}_0, \tag{C.1}$$

$$\boldsymbol{B}_0 = \nabla \times \boldsymbol{A}_0, \tag{C.2}$$

$$\boldsymbol{J}_0 = \sigma \boldsymbol{E}_0, \tag{C.3}$$

where $\boldsymbol{J}_0$ is the current field, $\boldsymbol{A}_0$ is the magnetic vector potential produced by the magnetized materials and $\boldsymbol{E}_0$ is the electric displacement field. The constitutive relation

$$\boldsymbol{B}_0 = \mu_0 \mu_r \boldsymbol{H}_0 \tag{C.4}$$

is applied to the aluminum plates ($\mu_r^{Al} = 1.000022$), surrounding air ($\mu_r^{air} = 1$) and copper coils ($\mu_r^{Cu} = 1$). Within the ferrofluid volume, the constitutive

relation is defined by the magnetization curve $M = f(H)$ depicted in Figure 4, that results in

$$\boldsymbol{B}_0 = \mu_0 \left(1 + \frac{f(H_0)}{H_0}\right) \boldsymbol{H}_0, \tag{C.5}$$

where H_0 is the module of the magnetic field $\boldsymbol{H}_0$. The ferrofluid volume is modeled as a cylinder of 110 mm diameter and 50 mm height, neglecting the contribution of the oscillating free surface. This approximation is consistent with the low susceptibility of the ferrofluid solution and its small impact on the magnetic field $\boldsymbol{H}_0$. Finally, the current field is computed through

$$\boldsymbol{J}_0 = \frac{NI}{A} \boldsymbol{e}_{coil}, \tag{C.6}$$

with $N = 200$ being the number of turns, $I = 16.11$ A the current intensity flowing through each wire, $A = 509$ mm^2 the coils cross section and $\boldsymbol{e}_{coil}$ the circumferential vector.

The simulation domain is a rectangular 1×3 m region enclosing the assemblies. An axisymmetric boundary condition is applied to the symmetry axis, while the tangential magnetic potential is imposed at the external faces through $\boldsymbol{n} \times \boldsymbol{A}_0 = \boldsymbol{n} \times \boldsymbol{A}_d$. $\boldsymbol{A}_d$ is the dipole term of the magnetic vector potential generated by the magnetization fields of the coils and ferrofluid volumes. Consequently, $\boldsymbol{A}_d$ is computed as the potential vector generated by four point dipoles applied at the centers of the magnetization distributions and whose moments are those of said distributions. While the dipoles associated to the coils can be calculated beforehand, the ferrofluid dipoles need to be approximated iteratively by integrating $\boldsymbol{M}$ in the ferrofluid volume. The relative error in the magnetic vector potential due the dipole approximation is estimated to be below 1.0% at the boundary of the domain with respect to the exact value generated by equivalent circular loops.

The mesh is composed by 3225100 irregular triangular elements shown in Figure C.9. Mean and minimum condition numbers of 0.955 and 0.644 are measured.

The fields $\boldsymbol{H}_0$ (shown in Figure C.10), $\boldsymbol{B}_0$ and $\boldsymbol{M}_0$ represent the main output from the previous model. In order to compute the total forces in the droplet volume and surface, given by Eq. (12), Eq. (17) and Eq. (19), the internal fields $\boldsymbol{H}$ and $\boldsymbol{M}$ have to be first obtained. The droplet is considered to be spherical, since the magnetic Bond number,

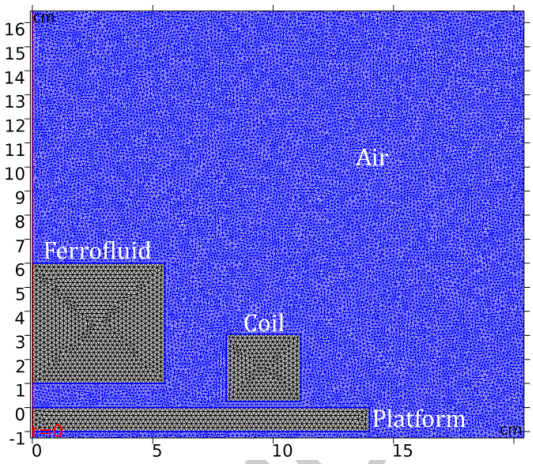

Figure C.9: Mesh of the magnetic field FEM model. An identical assembly is implemented 368 mm below. The simulation domain is a 1×3 m rectangular region enclosing both elements.

defined by

$$Bo_m = \frac{\mu_0 H^2 R}{\sigma}, \tag{C.7}$$

is approximately equal to 0.4. Consequently, surface tension dominates over the magnetic component, giving rise to the quasi-spherical equilibrium surface observed in Figure 2.

Within the magnetized medium, the applied and internal magnetic fields are related through $\boldsymbol{H} = \boldsymbol{H}_0 + \boldsymbol{H}_d$, where the demagnetization field $\boldsymbol{H}_d$ is approximated as $\boldsymbol{H}_d = -D\boldsymbol{M}$, D being the demagnetization factor. Considering the linearity of the fields $\boldsymbol{H}$, $\boldsymbol{M}$ and $\boldsymbol{H}_0$ inside the droplet and the magnetization curve $M = f(H)$, the relation

$$H + D\, f(H) = H_0 \tag{C.8}$$

has to be satisfied. This expression allows computing the fields $\boldsymbol{H}$ and $\boldsymbol{M}$ inside the droplet and then the total forces in the droplet volume and surface, given by Eq. (12), Eq. (17) and Eq. (19).

An exact value of D can only be obtained for ellipsoidal geometries subjected to uniform fields, being necessary to perform analytical approximations or numerical simulations for other cases [38]. However, given the small size of the droplet with respect to the system and the smooth variation of $\boldsymbol{H}_0$ observed in Figure C.10, a demagnetization factor $D = 1/3$, corresponding to a sphere, is assumed.

Based on Eq. (21), the characteristic time of change of the magnetic field is estimated to be 6 s for a reference field of 2500 A/m. Since the ratio

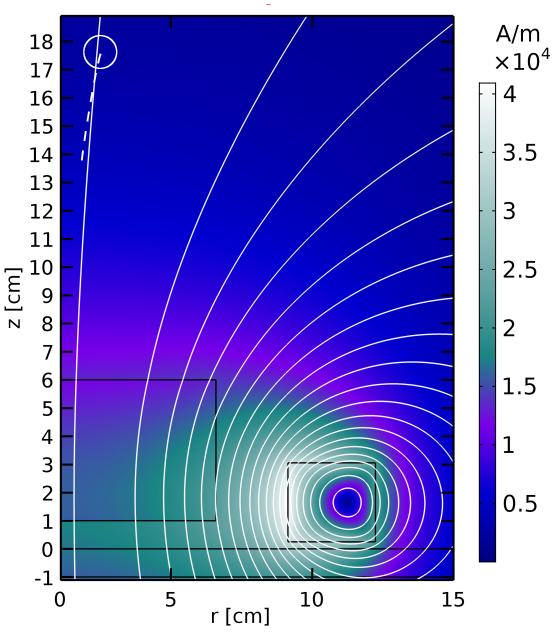

Figure C.10: Representation of the magnetic field $\boldsymbol{H}_0$ lines and intensity computed with Comsol Multiphysics at the upper assembly and path of the droplet. The color map shows the magnetic field intensity H_0, while the black contours represent the ferrofluid volume, coil and aluminum platform.

$\tau_f/\tau \approx 10^9$, the system is subjected to a magnetostatic process. Finally, the thermodynamic quasi-equilibrium condition can be assumed due the absence of relevant magnetodisipative effects.

Eq. (5) can be implemented by considering that the normal component of $\boldsymbol{B}$ and the tangential component of $\boldsymbol{H}$ are continuous in the droplet interface, and that the external medium is non-magnetic. Then, the *stress vector* $\boldsymbol{t}_n^+$, integrand of Eq. (5), results to be

$$\boldsymbol{t}_n^+ = \boldsymbol{n} \cdot \mathcal{T}_m^+ = B_n \boldsymbol{H}^- - \frac{\mu_0}{2}\left[\left(H^-\right)^2 - M_n^2\right]\boldsymbol{n} \tag{C.9}$$

and can be computed by assuming the relation given by Eq. (C.8). This is valid for the canonical and dual formulations of $\mathcal{T}_m$ shown in Eq. (2) and Eq. (13).

References

[1] C. Rinaldi, H. Brenner, Body versus surface forces in continuum mechanics: Is the maxwell stress tensor a physically objective cauchy stress?, Phys. Rev. E 65 (2002) 036615.

[2] M. Liu, K. Stierstadt, Colloidal Magnetic Fluids, 2009.

[3] S. Odenbach, M.Liu, Invalidation of the kelvin force in ferrofluids, Physical Review Letters 86 (2001) 328.

[4] A. Engel, Comment on "invalidation of the kelvin force in ferrofluids", Phys. Rev. Lett. 86 (2001) 4978–4978.

[5] M. Liu, Liu replies, Phys. Rev. Lett. 86 (2001) 4979.

[6] A. Lange, Kelvin force in a layer of magnetic fluid, Journal of Magnetism and Magnetic Materials 241 (2) (2002) 327 – 329.

[7] M. Petit, A. Kedous-Lebouc, Y. Avenas, M. Tawk, E. Arteaga, Calculation and analysis of local magnetic forces in ferrofluids, Przeglad Elektrotechniczny (Electrical Review) 87 (2011) 115–119.

[8] A. Engel, R. Friedrichs, On the electromagnetic force on a polarizable body, American Journal of Physics 70 (4) (2002) 428–432.

[9] A. F. Bakuzis, K. Chen, W. Luo, H. Zhuang, Magnetic body force, International Journal of Modern Physics B 19 (07n09) (2005) 1205–1208.

[10] J. C. Boulware, H. Ban, S. Jensen, S. Wassom, Influence of geometry on liquid oxygen magnetohydrodynamics, Experimental Thermal and Fluid Science 34 (8) (2010) 1182 – 1193.

[11] J. Martin, J. Holt, Magnetically actuated propellant orientation experiment, controlling fluid motion with magnetic fields in a low-gravity environment, NASA/TM-2000-210129, M-975, NAS 1.15:210129.

[12] D. Shi, Q. Bi, Y. He, R. Zhou, Experimental investigation on falling ferrofluid droplets in vertical magnetic fields, Experimental Thermal and Fluid Science 54 (April) (2014) 313 – 320.

[13] P. Poesio, E. Wang, Resonance induced wetting state transition of a ferrofluid droplet on superhydrophobic surfaces, Experimental Thermal and Fluid Science 57 (2014) 353 – 357.

[14] M. E. Moghadam, M. B. Shafii, E. A. Dehkordi, Hydromagnetic micropump and flow controller. part a: Experiments with nickel particles added to the water, Experimental Thermal and Fluid Science 33 (2009) 1021 – 1028.

[15] S. Papell, Low viscosity magnetic fluid obtained by the colloidal suspension of magnetic particles, US Patent 3215572.

[16] J. L. Neuringer, R. E. Rosensweig, Ferrohydrodynamics, The Physics of Fluids 7 (12) (1964) 1927–1937.

[17] R. E. Rosensweig, Ferrohydrodynamics, Dover Publications, 1997.

[18] D. Ludovisi, S. S. Cha, N. Ramachandran, W. M. Worek, Heat transfer of thermocapillary convection in a two-layered fluid system under the influence of magnetic field, Acta Astronautica 64 (11) (2009) 1066 – 1079.

[19] A. Bozhko, G. Putin, Thermomagnetic convection as a tool for heat and mass transfer control in nanosize materials under microgravity conditions, Microgravity Science and Technology 21 (1) (2009) 89–93.

[20] A. Causevica, P. Sahli, F. Hild, K. Grunwald, M. Ehresmann, G. Herdrich, Papell: Interaction study of ferrofluid with electromagnets of an experiment on the international space station, in: Proceedings of the 69th International Astronautical Congress, 2018.

[21] B. A. Jackson, K. J. Terhune, L. B. King, Ionic liquid ferrofluid interface deformation and spray onset under electric and magnetic stresses, Physics of Fluids 29 (6) (2017) 064105.

[22] K. Lemmer, Propulsion for cubesats, Acta Astronautica 134 (2017) 231 – 243.

[23] J. G. Marchetta, A. P. Winter, Simulation of magnetic positive positioning for space based fluid management systems, Mathematical and Computer Modelling 51 (9) (2010) 1202 – 1212.
[24] A. Romero-Calvo, G. Cano Gómez, E. Castro-Hernández, F. Maggi, Free and Forced Oscillations of Magnetic Liquids Under Low-Gravity Conditions, Journal of Applied Mechanics 87 (2), 021010.
[25] L. Landau, E. Lifshitz, Electrodynamics of Continuous Media, Pergamon Press, 1960.
[26] W. Panofsky, M. Phillips, Classical Electricity and Magnetism, Addison–Wesley Publishing Co., 1962.
[27] J. Jackson, Classical Electrodynamics, John Wiley, 1998.
[28] D. Griffiths, Introduction to Electrodynamics, Prentice–Hall, 1999.
[29] J. A. Stratton, Electromagnetic Theory, McGraw-Hill, 1941.
[30] J. Melcher, Continuum Electromechnanics, MIT Press, 1981.
[31] R. E. Rosensweig, Continuum equations for magnetic and dielectric fluids with internal rotations, The Journal of Chemical Physics 121 (3) (2004) 1228–1242.
[32] M. Liu, Range of validity for the kelvin force, Phys. Rev. Lett. 84 (2000) 2762.
[33] I. Torres-Díaz, C. Rinaldi, Recent progress in ferrofluids research: novel applications of magnetically controllable and tunable fluids, Soft Matter 10 (2014) 8584–8602.
[34] A. Romero-Calvo, T. H. Hermans, L. P. Benítez, E. Castro-Hernández, Drop Your Thesis! 2017 Experiment Report - Ferrofluids Dynamics in Microgravity Conditions, European Space Agency - Erasmus Experiment Archive, 2018.
[35] A. Romero-Calvo, T. Hermans, G. Cano Gómez, L. Parrilla Benítez, M. A. Herrada Gutiérrez, E. Castro-Hernández, Ferrofluid dynamics in microgravity conditions, in: Proceedings of the 2nd Symposion on Space Educational Activities, 2018.
[36] A. Myshkis, R. Wadhwa, Low-gravity fluid mechanics: mathematical theory of capillary phenomena, Springer, 1987.
[37] D. Scaramuzza, A. Martinelli, R. Siegwart, A toolbox for easily calibrating omnidirectional cameras, in: 2006 IEEE/RSJ International Conference on Intelligent Robots and Systems, Benjing, China, 2006, pp. 5695–5701.
[38] B. Pugh, D. Kramer, C. Chen, Demagnetizing factors for various geometries precisely determined using 3-d electromagnetic field simulation, IEEE Transactions on Magnetics 47 (10) (2011) 4100–4103.